www.czasopisma.pan.pl PAN POLSKA AKADEMIA NAUK www.journals.pan.pl

Arch. Metall. Mater. **68** (2023), 2, 681-688

DOI: https://doi.org/10.24425/amm.2023.142449

R.F. ASSUMPÇÃO[1*], J.C. FORTES MONTEIRO[2], V.C. CAMPIDELI[2], D.B. SANTOS[1], D.C. SICUPIRA[2]

INFLUENCE OF AGING TIME AT 850°C ON MICROSTRUCTURE AND CORROSION RESISTANCE OF A COLD ROLLED 2205 DUPLEX STAINLESS STEEL

The effect of aging time at 850°C for 300 s, 600 s, 1800 s, and 84600 s on the microstructural evolution and corrosion resistance of 2205 duplex stainless steel (DSS) was studied after cold rolling up to 60% of reduction. X-ray diffraction, scanning electron and transmission electron microscopy were used for microstructural characterization. The corrosion behavior was studied by cyclic potentiodynamic polarization (CPP) and electrochemical impedance technique (EIS) in 3.5% NaCl solution and the susceptibility to sensitization was investigated through the double loop electrochemical potentiodynamic reactivation (DL-EPR) test in 0.5 M H_2SO_4 + 0.1 M NaCl + 0.002 M KSCN solution. After cold working, increasing aging time led to an increase in sigma phase precipitation and a decrease in pitting corrosion resistance. However, the ultrafine microstructure had a beneficial influence on the self-healing effect in Cr and Mo depleted areas with the increasing of aging time, resulting in higher passivation ability. The DSS 2205 type was not susceptible to intergranular corrosion for the aged conditions applied.

Keywords: Duplex stainless steel; Aging; Corrosion; Secondary phases; Self-Healing

1. Introduction

Duplex stainless steels (DSS) are characterized by a microstructure consisting of ferrite (α) and austenite (γ) arranged as parallel lamellae after mechanical working [1]. Duplex stainless steels are widely used in industries due to their high strength and excellent corrosion resistance [2]. When DSS is exposed to temperatures ranging from 300°C to 1000°C, deleterious phases may precipitate, such as intermetallic phases and nitrides [3]. The nose of the precipitation-temperature-time (PTT) curve for the 2205 steel is located near 850°C [4], which indicates higher precipitation kinetics. Sigma (σ) phase results from a eutectoid reaction ($\alpha \rightarrow \sigma + \gamma_2$) or directly from ferrite ($\alpha \rightarrow \sigma$) [5]. Although, several studies have reported the quantification, kinetics, and mechanism of σ phase formation, few of them [5-7] have treated this phase transformation after hot or cold work, and in this direction, there are even fewer research that dealt with a DSS with ultrafine grains (1-3 µm) [5].

Precipitates rich in Cr and Mo are suggested to result in lower corrosion resistance due to the consumption of these beneficial passivating elements of the matrix [8]. However, the self-healing of sensitization was often found in conventional austenitic stainless steels [9,10] and some duplex stainless steels [11-13]. Nonetheless, due to the various types of materials, processing routes and heat treatments conditions, the results related to self-healing in DSS are somewhat controversial. Jin-long et al. [9] works indicates that self-healing in AISI 304 austenitic stainless steel can be effectively accelerated by cold-rolling. To the author's knowledge, no studies were found relating cold deformation before aging in 2205 DSS.

The objectives of the present work were to investigate the effect of cold rolling and aging time on the microstructure of a DSS, on the sigma phase isothermally transformed and on the corrosion properties. Thus, the effect of aging time at 850°C on the evolution of the microstructure and corrosion resistance of a cold rolled 2205 DSS was investigated by scanning electron microscopy (SEM), transmission electron microscopy (TEM), X-ray diffraction (XRD) and microhardness measurements. Corrosion behavior was evaluated by Cyclic potentiodynamic polarization (CPP) and Electrochemical impedance spectroscopy (EIS) in 3.5% NaCl solution, and by double loop electrochemical potentiodynamic reactivation (DL-EPR) tests in 0.5 M H_2SO_4 + 0.1 M NaCl + 0.002 M KSCN.

[1] UNIVERSIDADE FEDERAL DE MINAS GERAIS, DEPARTMENT OF METALLURGICAL AND MATERIALS ENGINEERING, BELO HORIZONTE, BRAZIL
[2] UNIVERSIDADE FEDERAL DE OURO PRETO, DEPARTMENT OF CHEMISTRY, CAMPUS MORRO DO CRUZEIRO, BRAZIL

* Corresponding author: raphaafranca@hotmail.com

2. Materials and Experimental Procedures

Hot rolled 2205 duplex stainless steel homogenized at 1100°C for 300 s with chemical composition as shown in TABLE 1 was used for the investigation. The material was cold rolled at room temperature to reach a 60% thickness reduction. Subsequently, the samples were aged at 850°C for 5, 10, 30 min, and 24 h in a muffle furnace and then cooled in water.

TABLE 1

Chemical composition of the steel (wt %)

Element	C	Mn	Si	Cr	Ni	P	S	Mo	Cu
wt%	0.013	1.81	0.38	22.45	5.31	0.02	0.0005	2.63	0.24

The microstructure characterization was done by scanning electron microscopy (SEM) and transmission electron microscopy (TEM). The SEM samples were prepared according to a standard metallographic procedure and etched with Beraha etchant. Thin foils used for observation by TEM were prepared by single-jet electropolishing in a solution of 5% perchloric acid and 95% methanol at approximately −30°C and a voltage of 20 V. The foils were examined using a TEM FEI Tecnai G2-20 operating at 200 kV. Aging time of 24 h and 30 min were chosen to be analyzed by TEM. Selected area diffraction (SAED) patterns were obtained for phase identification in both samples. X-ray diffraction (XRD) was also used for phase identification and semi-quantification. The integral of the area under the diffraction peaks were used to calculate the volume fraction of each phase using OriginProTM software. Microhardness measurements were performed using a load of 500 gf and indentation time of 15 s. Twenty measurements were done for each sample. The results reported correspond to mean value of these measurements.

Electrochemical measurements were recorded on a Autolab PGSTAT302N potentiostat by the three-electrode system at 22 ± 2°C. An Ag/AgCl (sat.) reference electrode and platinum plate as counter were connected to electrochemical workstation. The samples were mounted in acrylic resin, ground to 600 grit silicon carbide paper and the contact region between the sample and resin was sealed with araldite epoxy. All electrochemical tests were initiated after 60 min of immersion for open circuit potential (OCP) stabilization.

CPP and EIS were carried out in a 3.5% NaCl solution. CPP curves were performed using a sweep rate of 1.0 mV s^{-1}. Their scan direction was reversed when the current density reached 1200 $mV_{Ag/AgCl}$ or 1.0 mA cm^{-2}. The EIS analysis was performed at frequency range of 100 kHz to 5 mHz with 10 points per decade with 10 mV sinusoidal perturbation. The DL-EPR test consisted of performing an anodic scan starting from the OCP to a potential of +300 $mV_{Ag/AgCl}$ and subsequently reversing the scan to the open circuit potential again. The sweep rate in both directions was 1.0 mV s^{-1} in solution containing 0.5 M H_2SO_4 + 0.1 M NaCl + 0.002 M KSCN.

3. Results and discussion

3.1. Microstructural analysis

The microstructure of the as-received and cold rolled samples are presented in Fig. 1a,b, respectively. For the micrographs obtained with SEM, the presence of ferrite (dark gray phase) and austenite (light gray phase) can be observed. The contrast between the phases is not so pronounced in the SEM images in secondary electron mode, (SEI), so the phase identification can be better using the backscattered electrons mode, (BEI), as presented in Fig. 2. It was used a light etch with Behara etchant that preferentially reveals α phase and emphasizes the γ phase. The hot rolling, Fig. 1a, resulted in a partially work hardened microstructure of alternating austenite and ferrite grains, elongated in the rolling direction. After cold rolling, Fig. 1b, grain refining was observed with reduction in phase spacing and lamella thickness.

Fig. 2a-c illustrates the micrographs of the aged samples at 850°C for 300 s, 600 s, and 86400 s (24 h). Some elongated structures are verified in the α/γ interphase at all aging times. These microstructures are characteristic of the sigma phase and their chemical analyses are listed in TABLES 2 and 3. In addition, it is observed that increasing aging time led to a decrease

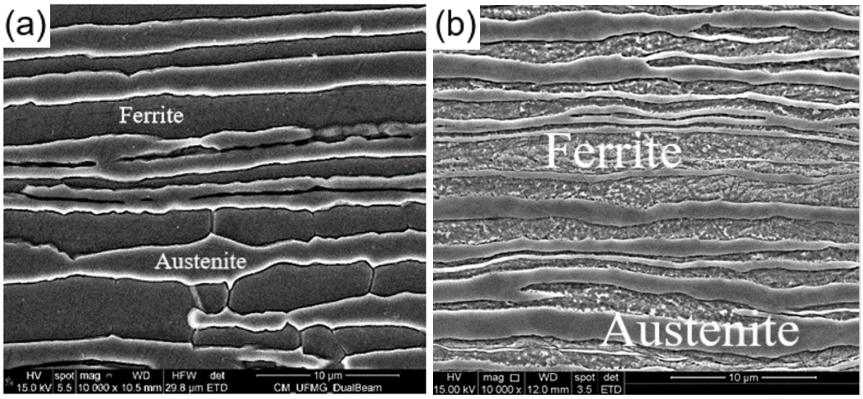

Fig. 1. SEM micrographs obtained using secondary electrons image (SEI) of the 2205 DSS (a) as-received condition and (b) cold rolled, longitudinal section

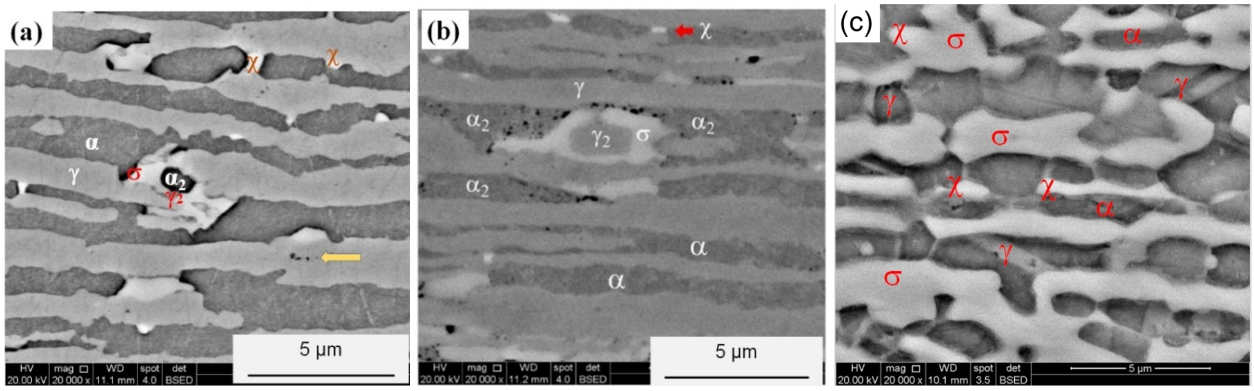

Fig. 2. SEM micrographs of backscattered electron image (BEI) of the 2205 DSS aged at 850ºC (a) for 300 s, (b) for 600 s, and (c) for 86400 s

in volume fraction of the ferrite phase. This is due to the eutectoid decomposition of ferrite, whose products are the sigma phase and secondary austenite, γ_2, Fig. 2b for instance. Under etching, pits (black particles – yellow arrow) are nucleated in the interior of the austenite grain, Fig. 2(a). As the ferrite transforms to σ phase, the surrounding ferrite (α_2) becomes reduced in Cr and Mo content, with intense pitting formation, as depicted in Fig. 2b and TABLE 2. However, with the microstructure changes from aging for 600s to 86400s no pits were observed, indicating increase in corrosion resistance, Fig. 2c. The sigma phase grows at the expense of α_2 and at the same time a coalescence process takes place with the elimination of boundaries between the neighboring grains, Fig. 2a-c. The matrix in the dark gray color is now almost completely austenitic, Fig. 2c and TABLE 3.

TABLE 2

EDS measurements of the phases identified in Fig. 2a,b

Phase / Elements	Si	Mo	Cr	Mn	Fe	Ni	Label in
Ferrite (α)	0.8	4.4	25.4	1.9	63.7	3.9	Fig. 2(a)
Austenite (γ)	0.8	2.3	21.7	2.1	66.5	6.7	Fig. 2(a)
Sigma (σ)	0.9	5.9	27.3	1.8	60.6	3.5	Fig. 2(a)
Chi (χ)	1.3	8.5	23.6	1.8	59.9	4.8	Fig. 2(a)
α_2	0.8	2.9	25.0	2.1	65.7	3.5	Fig. 2(b)
γ_2	0.7	3.1	23.1	1.9	66.5	4.7	Fig. 2(b)
Sigma (σ)	0.9	6.6	28.4	1.8	58.9	3.5	Fig. 2(b)

TABLE 3

EDS measurements of the phases identified in Fig. 2c

Phase / Elements	Si	Mo	Cr	Mn	Fe	Ni
Austenite	0.97	2.23	19.78	2.16	66.83	6.82
Sigma	0.87	6.10	29.6	2.02	57.86	3.55

Chemical analysis, performed by energy dispersive spectroscopy (EDS), are listed in TABLE 2, indicated that the α phase is enriched in elements such as Cr and Mo, and the γ phase is enriched in Ni and Mn. Moreover, the Cr and Mo contents in σ phase and Mo in χ phase were much higher compared with those in α and γ phases. However, γ_2 phase was enriched in Ni, and depleted in Cr compared to α and σ. Generally, the appearance of γ_2 phase could be expected to decrease the corrosion resistance, due the usually lower Cr content. However, a higher content of Cr and Mo in γ_2 phase appeared after aging up to 600 s. Gong et al. [14] also noticed an enrichment of γ_2 phase after aging a 2205 DSS at 800°C from 24 h to 48 h.

Fig. 3 and 4 are TEM micrographs of the samples aged for 1800 s and 86400 s, there are also selected area diffraction patterns (SADP) that identify σ-phase particles and austenite.

Fig. 5a-e shows the XRD pattern of the samples as-received, cold rolled and aged for 1800 s and 86400 s. The intensity of secondary phases and austenite increases with aging time. On the contrary, the volume fraction of ferrite decreases. The quantifi-

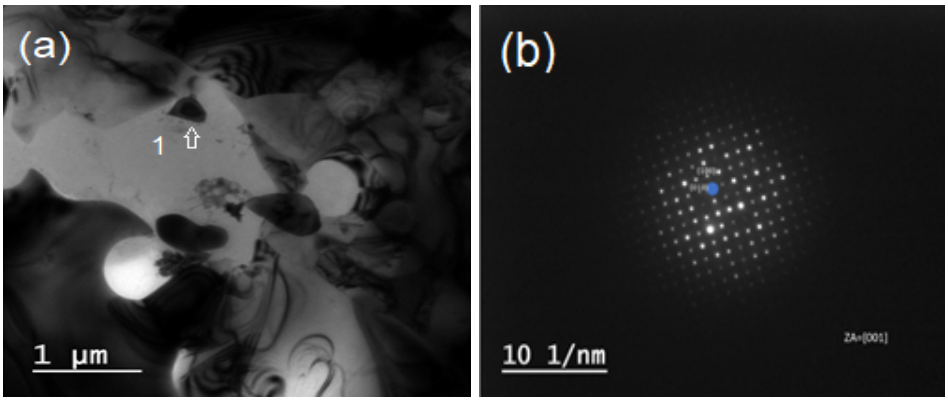

Fig. 3. (a) TEM micrograph of 2205 DSS annealed at 850°C for 1800 s. (b) Selected area diffraction pattern (SADP) correspondent to point 1 in (a), showing the [001] zone axis of the σ phase

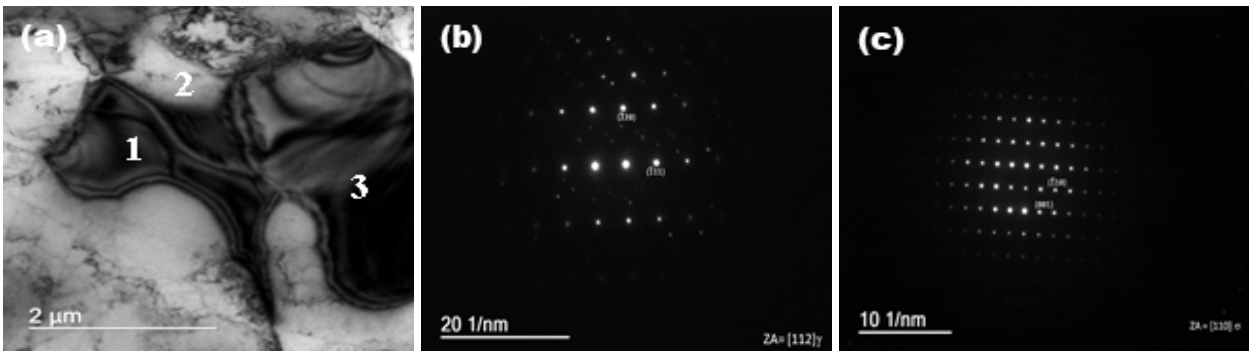

Fig. 4. (a) TEM micrographs of the 2205 DSS aged at 850°C for 86400 s. (b) SADP of the austenite, taken along the [112] zones axis (point 2). (c) SADP of the σ-phase taken along the [110] zone axis (point 1)

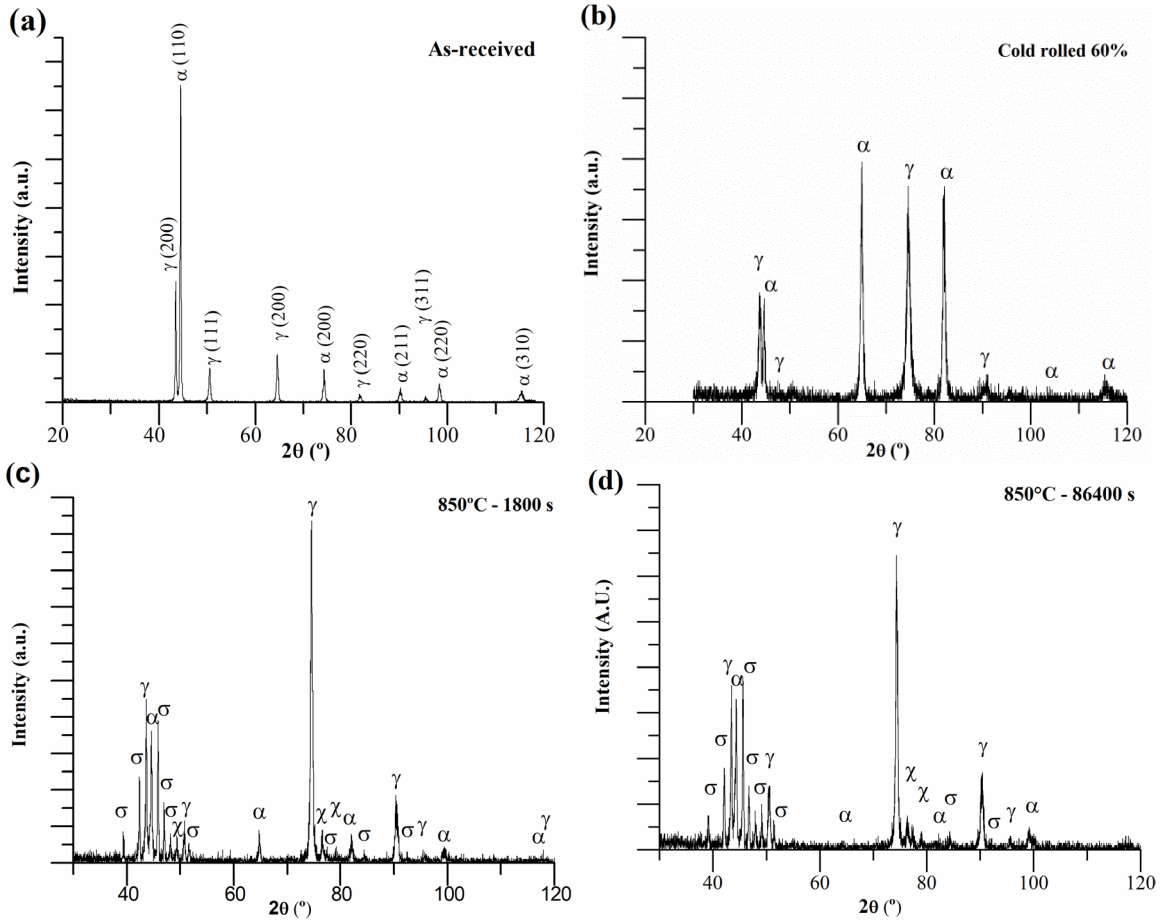

Fig. 5. Diffraction patterns of the 2205 DSS (a) as-received condition (that is industrial hot rolling and homogenized at 1050°C for 300 s, and then water cooled); (b) cold rolled condition; (c) aged at 850°C for 1800 s; (d) aged at 850°C for 86400 s; (e) detail of the region outlined in (d)

cation of the phases for each processing condition is presented in TABLE 4. As aging time increased, the amounts of σ and γ phases were enhanced and the amount of α phase decreased, as presented in TABLE 2.

Aging temperature of 850°C favors the χ phase precipitation for shorter soaking time, 300 s, TABLE 4, however, due the small amount of χ phase the phase quantification is restricted by the x-ray diffraction detection limit. The nucleation of χ, occurred preferentially at the α/α and α/γ interfaces, as shown in Fig. 2b,c. Prolonged soaking times should lead to the transformation of

TABLE 4

Phase volume fraction, Vv (%), of DSS samples 2205 after cold rolling and aging

Phase		850°C – Time (s)			
	CR	300	600	1800	86400
σ	—	6	13	18	22
γ	46	53	59	63	63
α	54	39	25	16	13
χ	—	<2	<2	<2	<2

χ into sigma [3,15], but this transformation was not observed here even aging for 24 h. Llorca-Isern et. al [16], reported the χ-phase precipitation after aging a solution treated 2205 for 9 h at 830°C. Gao et al. [17] investigated the same duplex stainless type and found χ phase after aging a hot rolled and a cold rolled 2205 DSS at 850°C for 4 h.

For 24 h aging time the presence of the σ phase is dominant in relation to ferrite, in agreement with other authors [15]. As we can observe, the longer the time higher is the σ-phase volume fraction following the eutectoid ferrite decomposition according to the reaction $\alpha \rightarrow \sigma + \gamma_2$. However, although this type of precipitation was observed, the characteristic eutectoid morphology, lamellar arrange, was not observed. The σ phase can form directly from ferrite and consume this phase, leaving a α_2 phase depleted in Cr and Mo and thus became more prone to corrosion attack, which was revealed by etching of the metallographic sample. This result can be observed in Fig. 2b, α_2 region.

Cold working promoted the formation of the σ phase because recrystallized and cold working boundaries are nucleation sites for the σ phase at low temperatures. At high temperatures, fine recrystallized grains are formed and increased the area of the grain boundary facilitating the nucleation of σ phase. The volume fraction of σ phase is enhanced when the cold working reduction increases, consequently, the σ phase content increases. It was concluded that the defects of stacking fault, twin, and low angle grain boundaries acted as nucleation sites for σ phase [7,18].

TEM micrograph in Fig. 3 and 4 shows the σ phase precipitates in more detail as compared to the SEM images (Fig. 2). The calculation of the interplanar distances corroborated the identification made in Fig. 3b, and 4b,c. The coalescence process of σ phase is underway (Ostwald ripening), leading the system to acquire a more stable condition, Fig. 2c. The granular σ and χ phases get coarser according to Ostwald ripening and some coarse particles nucleate at $\alpha/\alpha/\gamma$ triple points and α/γ boundaries, which were observed to only grow towards ferrite (Fig. 2a-c). According to Escriba et al. [19], when the χ phase is completely surrounded by σ and the newly generated γ_2 phase, the χ particles began to disappear. Fig. 2a-c shows the presence of χ phase without σ precipitation on its surroundings. With further precipitation and growth of σ-phase is expected that χ-phase transforms to σ-phase.

Fig. 6 illustrates that after deformation the hardness changed from 248 HV for as received to 426 HV for cold rolling sample. This comes from work hardening imposed to the steel. At 850°C, the secondary phase precipitation become intense, although the recrystallization process was active, an increase in the hardness was observed. The amount of secondary phases present was high, 24% Vv, which is composed by 22% Vv of σ (TABLE 4), ~2% Vv of χ. As reported by Calliari et al. [20], the hardness sharply increased with the presence of 19%Vv of secondary phases. In the experiments carried out at 850°C for 600 s, 1800 s and 86400 s this behavior followed the same trend, since the volume fraction of the secondary phases increase, and the microstructure had already advanced in the recrystallization process. With the increase in the volume fraction of the secondary phases, the hardness increased, reaching 414 HV. It was observed that only ~8% Vv of secondary phases were enough to maintain the high Vickers hardness to 356 HV (aging for 300 s), indicating steel embrittlement. Certainly, the initial cold rolled microstructure contributed to this high value, and even after long ageing time of 24 h, remains with high dislocation density in the substructure of the sample, Fig. 4a. According to Reick et al. [21] the recrystallization of this kind of steel for such temperature (~850°C) start in the ferrite and after in the austenite. This condition certainly influences on corrosion behavior as will be addressed ahead.

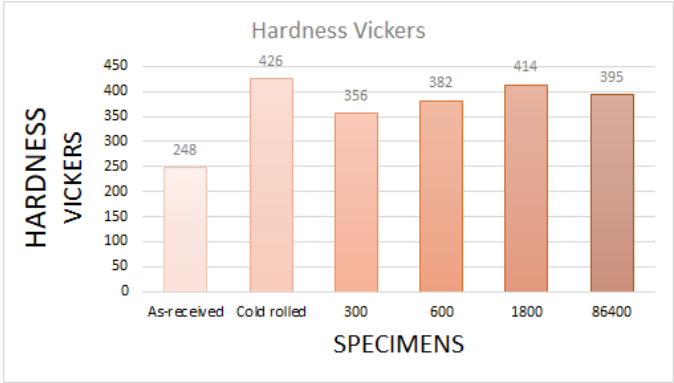

Fig. 6. Microhardness Vickers results for all processed samples

3.2. Electrochemical Ttsts

3.2.1. Electrochemical impedance spectroscopy technique

Fig. 7 shows representative CPP curves obtained for the 2304 DSS cold rolled up to 60%, and aged at 850°C for 300 s, 600 s, 1800 s and 84600 s. All five conditions exhibited passivity in the 3.5% NaCl solution. The passive current density increased with increasing potential for the treated samples, but remained on the order of 10^{-6} A cm^{-2}.

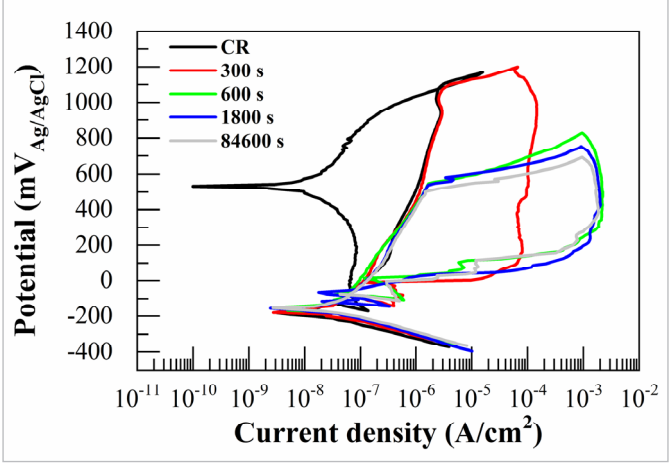

Fig. 7. CPP Typical CPP curves obtained representatives curves obtained on the samples: cold rolled 60% and annealed at 850°C for 300 s, 600 s, 1800 s, 86400 s, in a solution containing 3.5 wt.% NaCl

The reverse scan of the cold rolled sample showed a small positive hysteresis and a high repassivation potential, indicating that the sample has repassivation capacity. Large hysteresis loop and low repassivation potential, similar in value to the OCPs, was observed for 1800 s and 84600 s indicating that the chloride adsorbed on the metal surface can hindered the repassivation, resulting in formation of pits [2]. After aging for 300 s and 600 s the reverse scan did not intersect the passive region.

The pitting potential (Epit) of cold rolled and 300 s specimens had the highest values at 1100 ± 7 mV(Ag/AgCl) and 1090 ± 20 mV(Ag/AgCl), respectively. There was a clear degradation after aging for 600 s, pitting potential dropped to 550 ± 14 mV(Ag/AgCl). Despite the increase in the volumetric fraction of deleterious phases, no decrease in pitting potential was observed after aging for 1800 s. Nevertheless aging for 86400 s the pitting potential decreased from 545 ± 11 mV(Ag/AgCl) to 500 ± 4 mV(Ag/AgCl).

Fig. 8a-c shows the Nyquist and Bode diagram and the equivalent circuit used for data fitting. The Nyquist diagram, Fig. 8a, shows the correlation between real impedance and imaginary impedance at each frequency. Fig. 8b shows high phase angle values over a wide frequency range.

As can be seen from Fig. 8b, the Bode diagram has only one time constant (only a maximum at the phase angle in the mid-frequency region). Nyquist plots are all semi-circular arcs with centers depressed and are usually attributed to a mechanism of charge transfer on a heterogeneous surface. Small differences in the semicircle arcs can be observed for the different specimens in Nyquist plots. With increasing aging time, the diameter of the depressed semicircle increases. The equivalent circuit in Fig. 8c is proposed for fitting EIS data to quantify the electrochemical parameters. In this equivalent circuit, *Rs* represents solution resistance; CPE is the constant phase element and capacitance and *Rct* is the charge transfer resistance at the metal/electrolyte interface.

Aging for 300 s led to decrease of *Rct*, at this aging time recrystallization process was active. With recrystallization is expected improvements in corrosion resistance by grain refinement and removing the lattice curvature [11,22,23], however, sigma phase precipitation and partial recrystallization resulted in smaller corrosion resistance when compared to the cold rolled sample. Increasing aging time, kinetics of both recrystallization and phase precipitation was increased.

After 600 s and 84600 s the *Rct* value is similar to cold rolled sample and reached its higher value at 1800s. The large *Rct* values displayed by samples heat treated at 850°C for times larger than 600 s are unexpected. As discussed in previous works [23], increasing aging time led to increased precipitation of the sigma phase and this precipitation results in Cr and/or Mo depleted zones around it, which may result in decreased corrosion resistance of the duplex stainless steel 2205. The *Rct* values implies that their corrosion rate is similar or higher than that of the cold rolled sample, which is highly inconsistent with the results obtained by CPP test.

The same trend was observed by Chaves et al. [24], aging of a hot rolled and solution treated 2205 DSS at 850°C after 5 h, the *Rct* value surpassed that of the solution annealed sample, reaching values two times larger for samples aged for 20 h and 30 h. According to Chaves et al. [24], the higher *Rct* was due partially recovered regions by Cr and Mo diffusion from unaffected zones, making these regions less depleted in these elements and therefore the passive film resistance is not significantly affected.

In DSS, it has been shown that the sigma phase particles will keep growing and coalescing even after several thousand hours of annealing [25], the growing and coalescence of σ phase can also be observed in Fig. 2(a-c). As a result, σ phase particles

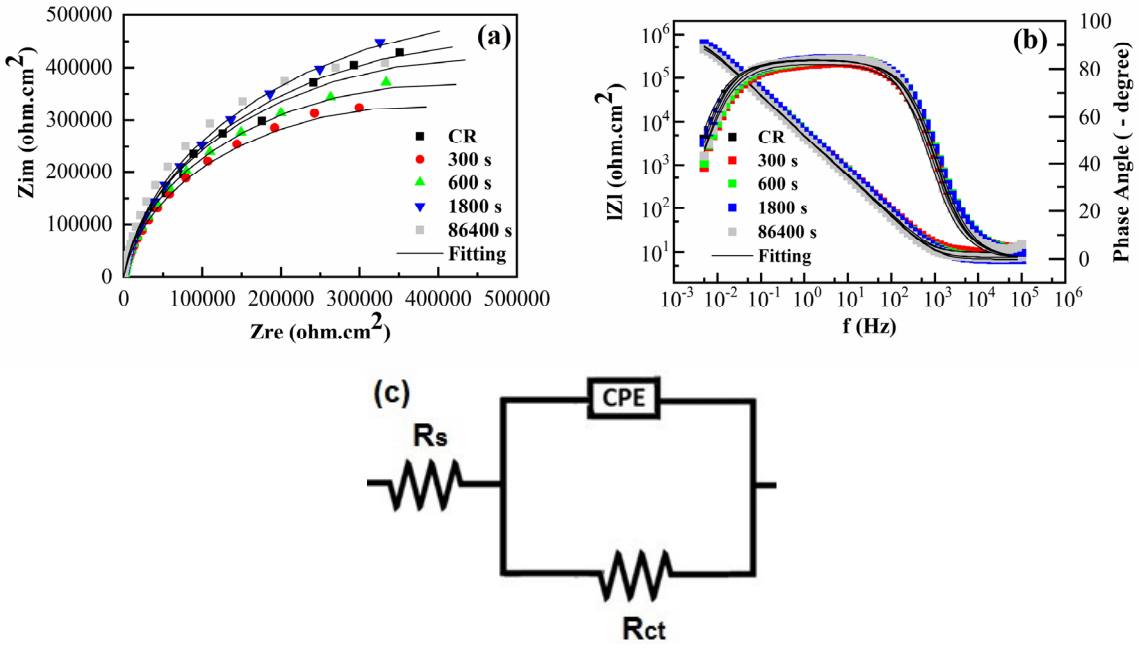

Fig. 8. (a) Nyquist diagram, (b) Bode diagram in 3.5 wt.% NaCl, and (c) equivalent circuit for EIS fitting where Rs is the resistance of the solution, CPE is the constant phase element and Rct is the charge transfer resistance at the metal/electrolyte interface

will keep sourcing Cr and Mo atoms from their vicinity even after prolonged annealing, however, the coalescence of σ phase also leads to lower surface area. Nevertheless, if the diffusion rate of Cr and Mo atoms from the matrix to the Cr- and Mo-depleted regions is higher than the depletion rate of Cr and Mo atoms due to sigma growth, the extent of Cr- and Mo-depleted zones will gradually decrease [13]. This phenomenon is named as self-healing [26].

Furthermore, in this study, aging the 2205 DSS at severely cold-worked state resulted at an ultrafine microstructure, as illustrated in Fig. 2a-c, and high dislocation density in the sub-structure of the aged samples, as observed in Fig. 6. Grain size can influence in the self-healing behavior, due to the massive diffusion channels caused by more grain boundaries in smaller grain size specimens [10,22]. Therefore, the availability of easy paths for Cr and Mo diffusion can result in quicker healing [26]. According to Riya Mondal et al. [22] by increased grain boundary density is expected to promote the diffusion of Cr to the surface, thereby leading to the formation of stable passive film.

Thus, the results shown in TABLE 5 may are related by the fact that the Cr- and Mo-depleted zones was healing up itself due to the diffusion of Cr and Mo from the σ phase to the γ_2 phase, which is consistent with the EDX results, presented in TABLE 2, it was observed that γ_2 had a higher amount of Cr and Mo than γ, consequently, the charge transfer through the passive film of the specimens after 600 s aging time will become more difficult. Similar results were observed by Gong et al. [14], after aging there was an indication of healing, decreasing the degree of sensitization value for solution threated 2205 specimens aged at 800°C with increasing aging time up to 48h, in this case, there was also an increase in the amount of Cr of γ_2 when compared with previous γ.

Fig. 9 shows the DL-EPR curves of CR samples thermally aged samples. Note that the reactivation current density peak was absent from the aged samples. The Qr/Qa ratio was calculated based on the areas under the activation scan curve (Qa) and the reactivation scan curve (Qr), results are illustrated in TABLE 6. The Qr/Qa ratio rises from CR to aged samples for 300 s due to the nucleation of the precipitates and high grain boundary precipitates size. After 600 s this value decreases due high rate of diffusional process of the alloying elements at the recrystallized fine microstructure from adjacent grains to depleted zones, recovering the depleted regions in Cr and Mo (mainly g_2 and primary ferrite, Fig. 2b and TABLE 2) and thus enabling the formation of a stable passive film. Qr/Qa ratio less than 1% are observed, indicating that steel under these conditions is not susceptible to intergranular corrosion.

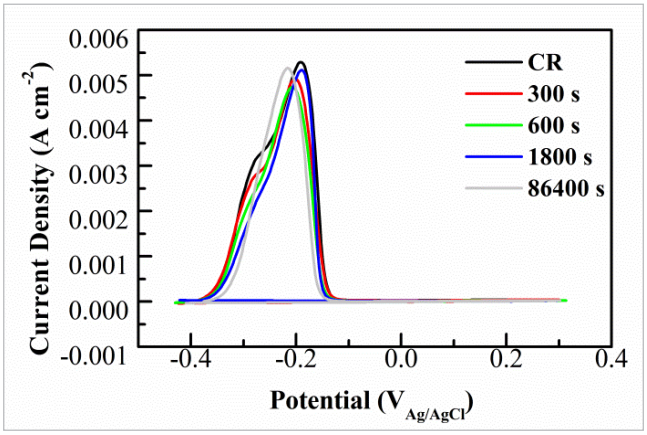

Fig. 9. DL-EPR curves in 0.5 M H_2SO_4 + 0.1 M NaCl + 0.002 M KSCN solution

TABLE 6

Average values of Qr/Qa and the respective deviation

Sample	Qr/Qa (%)	Deviation (%)
CR	0.43	0.04
300 s	0.98	0.11
600 s	0.93	0.04
1800 s	0.62	0.06
86400 s	0.48	0.03

Though sensitization and healing take place simultaneously their kinetics are different and are due to the difference in the rate of diffusion. The rate of diffusion along the grain boundaries is faster than the bulk diffusion and rate of healing is decided by the rate of Cr diffusion [26]. Zeng et al. [12] reported decrease in DOS value after 4 h of sensitization in a solution annealed 2205 DSS aged at 850°C from 10 min to 48 h and air-cooled, giving rise to weaker intergranular corrosion, even with increase of σ phase. Jin-long et al. [9] found that reactivation current in a AISI 304 austenitic stainless steel increased for 10% reduction as cold working increased up to 30% and 40% cold working, reactivation current decreases due to rapid healing. According to Shukla et al. [27] after thermal ageing of 50% cold work of a manganese austenitic stainless steel the DOS almost reached to the value of DOS of as received solution annealed sample with the advantage of having very less defects and recrystallized grains.

TABLE 5

EIS data adjustment parameters

Sample	R_s (Ω cm^2)		R_{ct} (Ω cm^2)		Q (Ω^{-1} cm^{-2} s^n)		n	
	Value	Deviation	Value	Deviation	Value	Deviation	Value	Deviation
CR	9.84	1.62	9.39E+05	2.64E+04	3.06E–05	1.31E–06	0.924	0.004
300 s	6.16	1.13	5.30E+05	2.36E+04	3.69E–05	1.88E–06	0.924	0.031
600 s	8.32	0.92	8.83E+05	8.79E+04	2.99E–05	4.46E–07	0.927	0.005
1800 s	7.26	0.54	1.04E+06	6.64E+04	3.05E–05	6.99E–07	0.930	0.001
86400 s	8.52	1.24	9.26E+05	3.49E+04	2.88E–05	1.38E–06	0.931	0.018

4. Conclusions

The corrosion behavior of DSS 2205 aged at 850°C for various aging times were studied by microstructural characterization and electrochemical tests. Based on the obtained data the main findings of this research are as follows:

- The σ and χ phases nucleate simultaneously at the initial stages of aging. The volume fraction of sigma phase increased with aging time. However, the χ phase stayed stable and did not decompose in σ phase, even for the longest aging time (86400 s).
- CPP curves showed that increasing aging time, pitting corrosion resistance decreases. However, EIS results exhibit small differences in the semicircle arcs for the specimens in the Nyquist plots. Increasing aging time, the charge transfer resistance slightly increases and becomes similar to the cold rolled sample. Moreover, DL-EPR test showed that 2205 DSS is not susceptible to intergranular corrosion under the studied conditions. The unexpected high charge transfer resistance of the aged samples and lack of sensitization was attributed to self-healing.
- After cold rolling, increasing aging time favored diffusional processes of passive layer forming elements such as Cr and Mo and therefore the corrosion resistance is not significantly affected. Grain refinement after cold rolling had a beneficial influence on the self-healing behavior due to the increase of diffusion paths.

Acknowledgements

The authors are grateful to Aperam South America for the steel samples supply. Also thank the CAPES-PPGEM/UFMG-REDEMAT/UFOP, CNPq and FAPEMIG for the student fellowship and financial support. Thanks to Centro de Microscopia – UFMG for transmission electron microscopy examination.

REFERENCES

[1] K.H. Lo, C.H. Shek, J.K.L. Lai, Mater. Sci. Eng. R Reports. **65**, 39-104 (2009).
[2] D.C. Sicupira, R.C. Junior, A.Q. Bracarense, S. Gerald, V.F.D. Lins, Mater. Res. **20**, 161-167 (2016).
[3] K.W. Chan, S.C. Tjong, Materials (Basel). **7**, 5268-5304 (2014).
[4] R. Magnabosco, Mater. Res. **12**, 321-327 (2009).
[5] V.A. Hosseini, L. Karlsson, S. Wessman, N. Fuertes, Materials (Basel). **11**, 933 (2018).
[6] V.C. Anelli, C. Gauss, D.R. Almeida, H.R.Z. Sandim, Pract. Metallogr. **55**, 319-343 (2018).
[7] H.S. Cho, K. Lee, Mater. Charact. **75**, 29-34 (2013).
[8] D.C. Sicupira, R. Cardoso Junior, A.Q. Bracarense, G.S. Frankel, V.F.D. Lins, Mater. Corros. **68**, 604-612 (2017).
[9] L. V. Jin-Long, L. Hong-Yun, Mater. Chem. Phys. **135**, 973-978 (2012).
[10] Q. Zhou, R. Wang, Z. Zheng, Y. Gao, Appl. Surf. Sci. **462**, 804-814 (2018).
[11] S. Shukla, A.P. Patil, A.P. Kawale, R.K. Haldkar, A. Dahiwale, A. Bansod, Mater. Today Proc. **44**, 2802-2807 (2021).
[12] H. Zeng, Y. Yang, R. Xu, S. Xin, M. Li, J. Solid State Electrochem. **23**, 2793-2801 (2019).
[13] L. Sun, Y. Sun, C. Lv, Y. Liu, N. Dai, Y. Jiang, J. Li, Corros. Sci. **185**, 109-432 (2021).
[14] J. Gong, Y.M. Jiang, B. Deng, J.L. Xu, J.P. Hu, J. Li, Electrochim. Acta. **55**, 5077-5083. (2010).
[15] A.D. Warren, R.L. Harniman, Z. Guo, C.M. Younes, P.E.J. Flewitt, T.B. Scott, J. Mater. Sci. **51**, 694-707 (2016).
[16] N. Llorca-Isern, H. López-Luque, I. López-Jiménez, M.V. Biezma, Mater. Charact. **112**, 20-29 (2016).
[17] T. Gao, J. Wang, Q. Sun, P. Han, Metals (Basel). 8 (2018).
[18] D.M.E. Villanueva, F.C.P. Junior, R.L. Plaut, A.F. Padilha, Mater. Sci. Technol. **22**, 1098-1104 (2006).
[19] D.M. Escriba, E. Materna-Morris, R.L. Plaut, A.F. Padilha, Mater. Charact. **60**, 1214-1219 (2009).
[20] I. Calliari, M. Zanesco, E. Ramous, J. Mater. Sci. **41**, 7643-7649 (2006).
[21] W. Reick, M. Pohl, A.F. Padilha, ISIJ Int. **38**, 567-571 (1998).
[22] R. Mondal, S. Kumar Bonagani, P. Raut, P. V. Sivaprasad, G. Chai, V. Kain, I. Samajdar, J. Electrochem. Soc. **167**, 101-501 (2020).
[23] L. Jinlong, L. Tongxiang, D. Limin, W. Chen, Corros. Sci. **104**, 144-151 (2016).
[24] R. Chaves, I. Costa, H.G. De Melo, S. Wolynec, Electrochim. Acta. **51**, 1842-1846 (2006).
[25] K.W. Wong, C.H. Shek, W. Zhang, J.K.L. Lai, Mater. Lett. **62**, 3991-3994 (2008).
[26] P. Rajesh Kannan, V. Muthupandi, K. Devakumaran, C. Sridivya, E. Arthi, Mater. Chem. Phys. **207**, 203-211 (2018).
[27] S. Shukla, A.P. Patil, Procedia Struct. Integr. **14**, 259-264 (2019).